



Non-invasive Monitoring of Ultrasound-Stimulated Microbubble Radiation Enhancement Using Photoacoustic Imaging

www.tcr.org
DOI: 10.7785/tcr.2013.600266

Modulation of the tumour microvasculature has been demonstrated to affect the effectiveness of radiation, stimulating the search for anti-angiogenic and vascular-disrupting treatment modalities. Microbubbles stimulated by ultrasound have recently been demonstrated as a radiation enhancer when used with different cancer models including PC3. Here, photoacoustics imaging technique was used to assess this treatment's effects on haemoglobin levels and oxygen saturation. Correlations between this modality and power doppler assessments of blood flow, and histology measurements of vascular integrity and cell death were also investigated. Xenograft prostate tumours in SCID mice were treated with 0, 2, or 8 Gy radiation combined with microbubbles exposed to 500 kHz ultrasound at a peak negative pressure of 0, 570, and 750 kPa. Tumours were assessed and levels of total haemoglobin, oxygen saturation were measured using photoacoustics before and 24 hours after treatment along with power doppler measured blood flow. Mice were then sacrificed and tumours were assessed for cell death and vascular composition using immunohistochemistry. Treatments using 8Gy and microbubbles resulted in oxygen saturation decreasing by $28 \pm 10\%$ at 570 kPa and $25 \pm 29\%$ at 750 kPa, which corresponded to $44 \pm 9\%$ and $40 \pm 14\%$ respective decreases in blood flow as measured with power doppler. Corresponding histology indicated $31 \pm 5\%$ at 570 kPa and $37 \pm 5\%$ at 750 kPa in terms of cell death. There were drops in intact vasculature of $15 \pm 2\%$ and $20 \pm 2\%$, for treatments at 570 kPa and 750 kPa. In summary, photoacoustic measures of total haemoglobin and oxygen saturation paralleled changes in power doppler indicators of blood flow. Destruction of tumour microvasculature with microbubble-enhanced radiation also led to decreases in blood flow and was associated with increases in cell death and decreases in intact vasculature as detected with CD31 labeling.

Key words: Photoacoustics; Anti-vascular therapy; Radiosensitizer; Ultrasound; Apoptosis; Cell death.

Introduction

Radiation therapy is a modality used in the treatment of many malignancies. Inducing cancer cell death directly by disruption of DNA is the primary mechanism of action of ionizing radiation. A second mechanism involves radiation-induced endothelial cell damage and endothelial cell death within the tumour

Abbreviations: CD31: Cluster of Differentiation 31; CT: Computed Tomography Scan; DNA: Deoxyribonucleic Acid; FDG: Fluorine-18 2-fluoro-2-deoxy-D-glucose; Gy (Gray): SI Unit of Radiation Dose; ISEL: *In-situ* End Labeling; MI: Mechanical Index; O2: Oxygen; PC3: Human Prostate Cancer Cell Line; PCR: Polymerase Chain Reaction; PET: Positron Emission Tomography Scan; SCID: Severe Combined Immunodeficiency; VI: Vascular Index.

Kaleigh Briggs^{1§}
Azza Al Mahrouki, Ph.D.^{1§}
Joris Nofiele, B.Sc.¹
Ahmad El-Falou, B.Eng.¹
Martin Stanisz¹
Hyunjung Christina Kim,
M.Sc.¹
Michael C. Kolios, Ph.D.³
Gregory J. Czarnota, Ph.D.,
M.D.^{1,2,4*}

¹Physical Sciences, Sunnybrook Research Institute, Toronto, ON, Canada

²Department of Radiation Oncology, Sunnybrook Health Sciences Centre, Toronto, ON, Canada

³Department of Physics, Ryerson University, Toronto, ON, Canada

⁴Departments of Radiation Oncology and Medical Biophysics, University of Toronto, Toronto, ON, Canada

[§]Equal contributions.

*Corresponding author:
Dr. Gregory J. Czarnota, Ph.D., M.D.
Phone: 416-480-6128
E-mail: Gregory.Czarnota@sunnybrook.ca

microvasculature leading indirectly to cancer cell death (1). Enhancing the effects of radiation by additional targeting of either of these pathways could translate to more effective treatments at less toxic doses. One method of increasing radiation tumour responses *in vivo* involves the use of ultrasound-mediated microbubbles to disrupt endothelial cells within tumour microvasculature (2-5).

Microbubbles are small (3-4 μm) bubbles of gas encased in a stabilizing lipid or protein coat. They are small enough to pass through microvasculature, but too large to extravasate through intact endothelial cell linings, making them good candidates for imaging vascular beds. In diagnostic ultrasound, microbubbles in circulation produce an acoustic impedance mismatch, a property which has been exploited for their use as contrast agents (6, 7). Low to moderate acoustic pressure (<200 kPa with a MI < 0.05) delivered from ultrasound results in microbubble oscillation. At higher acoustic pressures, pronounced expansion and contraction can lead to inertial cavitation and microbubble contrast agent destruction (8). The force of this destruction has the capacity to damage endothelial cell linings and cause capillary ruptures (9-11). A side effect to be avoided in diagnostics, this can be harnessed in the treatment of malignancies where microvascular damage within the tumour is desirable (12). We have previously demonstrated in prostate and bladder tumour xenografts models that this ultrasound-induced perturbation of tumour vasculature can result in increases of radiation-induced cell death. Experiments have demonstrated increased to 40-60% tumour cell death with a single 2 Gy fraction of radiation when combined with ultrasound-stimulated microbubble vascular perturbation with synergistic effects of the two treatments. The exact mechanism appears to be related to the induction of ceramide formation in endothelial cells which when combined with radiation causes increased levels of cell death. Experimentally, inhibition of this pathway chemically *in vitro* and *in vivo* inhibits the cell death inducing effects of microbubbles on endothelial cells. In addition, key molecules related to a cell-membrane and ceramide-induced cell death pathway have been identified by gene-expression analyses using gene-chip and quantitative-PCR methodologies (2-4). Effects of such treatments are recognized to cause creases in tumour blood flow due to the destruction of blood vessels. Although hypoxia can cause decreases in sensitivity to radiation in those treatments abrogation of blood flow causes an enhancement in cell death. Here we investigate the effects of these treatments using non-invasive monitoring using photoacoustic imaging methods.

Power doppler imaging has been used in the past to visualize tumour microvasculature damage after radiation and anti-angiogenic treatment (13) or combined ultrasound-mediated microbubble and radiation therapy (2), but photoacoustic

imaging represents an opportunity to overcome limitations of power doppler *in vivo*. One such limitation is the production of image artifacts (elevated noise from power doppler imaging motion artifact) caused by movement of tissues near blood vessels. In power doppler imaging of small vessels, necessary filter parameters allow such artifacts to escape filtering (14). The subjectivity of filter parameters and increased scatter signals formed by tissues near blood vessels also limits the resolution of power doppler for microvasculature imaging (14). Photoacoustics refers to the generation of acoustic waves or other thermoelastic effects by energetic radiation. Heat production caused by a pulsed laser of a specific wavelength produces a transient thermoelastic expansion influenced by the varying optical absorptions of biological tissues. The waves generated by this phenomenon can be captured with an ultrasound transducer to produce images. Photoacoustic imaging serves as a potential tool investigating tumour response to microbubble-based vascular disruption.

In photoacoustic imaging, blood acts as an endogenous contrast agent due to optical absorptions different to those of surrounding tissue. In addition to overcoming limitations of optical imaging caused by diffuse light-scattering, photoacoustic imaging also provides information beyond the scope of power doppler capabilities. Whereas power doppler imaging is sensitive to blood flow only, photoacoustic imaging is sensitive to both flowing and relatively static blood. Oxygenated and deoxygenated haemoglobin, and their relative concentrations, can also be distinguished with photoacoustic methods depending on the wavelength of the tissue-interrogating laser pulse (15).

The ability of photoacoustic imaging to select for physiological properties based on optical absorptions has been exploited in different ways, in particular for imaging vascularization and oxygenation of tissues. The imaging technology has been used in the identification of cancerous skin lesions as compared to vascular lesions (16-19), in the visualization of breast vasculature (20), for the detection of neovascular ocular disease (21), and for *in vivo* imaging of angiogenesis (19). It has also been used for the functional imaging of the nervous system via changes in blood volume, O_2 consumption and cellular swelling (22), and in the visualization of changing concentrations of oxygenated and deoxygenated haemoglobin (23).

In the study here photoacoustic imaging was used to investigate the disruption of blood vessels of tumour microvasculature with ultrasound-stimulated microbubble-enhanced radiation. Results correlated the findings to histopathology and doppler imaging and demonstrate the use of this technology in therapy response monitoring where blood-vessels and oxygen saturation are affected.

Materials and Methods

Cell Culturing and Generation of Xenograft Tumours

Human PC3, prostate cancer cells obtained from American Type Culture Collection (ATCC, Manassas, USA) were cultured in RPMI-1640 media, with 10% characterized serum (HyClone, South Logan, Utah, USA), and 100 U/ml of penicillin/streptomycin (Life Technologies, Burlington, ON, Canada). Tumours were grown in the hind leg of SCID-CB17 mice (Charles River, Senneville, QC, Canada) by injecting 1.0×10^6 cells subcutaneously. Treatments and imaging were carried out when tumours reached 7–8 mm diameter. Photoacoustic and power doppler imaging were performed before and 24 hours after treatment, as described further below. Four animals per experimental condition (described below) were used.

Ultrasound and Radiation Treatments

For treatments with ultrasound-stimulated microbubbles or radiation 70 μ l ketamine and xylazine (750 μ l of 150 mg/kg ketamine added to 250 μ l of 10 mg/kg xylazine and diluted in 4 ml saline) were used to anesthetize mice. Vialmix device-prepared definity microbubbles (perfluoropropane gas/liposome shell; Lantheus Medical Imaging) were administered at a concentration of 3.6×10^8 microbubbles in 30 mL volumes of prepared bubbles. The final circulating concentration was selected to be higher (100-fold) than the diagnostic dose. This dose was used to ensure efficient interactions of the bubbles and microvascular walls as before (2).

Mice were immersed in a 37°C water bath to permit ultrasound treatment and centered on the tumour. Ultrasound treatment was done as was previously described (2), tumours were exposed to acoustic waves as previously described (2), where tumours were subjected to a 16-cycle burst at a pulse repetition frequency of 3 kHz with a 10% duty cycle for a duration of 50 ms. This resulted in a 750 ms exposure over 5 minutes of treatment time, with an average duty cycle of 0.25%. This sequence was designed to allow blood vessels to refill with bubbles during a treatment time of 300 seconds (5 minutes) (2). For ultrasound exposures, a focused central frequency 500 kHz transducer (IL0509HP, ValpeyFisher Inc, MA) with a 28.6 mm transducer element diameter was used. This was attached to a micro-positioning system, and a waveform generator (AWG520, Tektronix, OR), a pulse-receive power amplifier (RPR4000, Ritec Inc, RI), and a digital-acquisition system (Acquiris CC103, Agilent Technologies, NY). The ultrasound peak negative pressure was 570 and 750 kPa for experiments measured with a calibrated hydrophone. The -6 dB beam-width was 31 mm and the -3 dB beam-width was 18 mm.

After ultrasound exposure, mice were lead-shielded and only tumour was exposed to ionizing radiation (Faxitron

Cabinet X-ray; Faxitron X-ray LLC) at doses of 0, 2, or 8 Gy in single fractions at a dose rate of 200 cGy/minute using 160 kVp X-rays. Mice were kept for 24 hours and then sacrificed for histopathology. Mice receiving no treatment, mice receiving only ultrasound-activated microbubbles, and mice receiving only radiation at doses of 2 and 8 Gy were used as controls.

There were nine treatment groups consisting of treatments of 0, 2, and 8 Gy combined each with microbubbles in the presence of 0, 570, and 570 kPa in sonifying ultrasound pressure.

Histopathology and Immunolabeling

Samples were fixed overnight at room temperature in 1% paraformaldehyde. Paraffin embedding, sectioning, and haematoxylin and eosin staining were done by the histology facility at Sunnybrook, Toronto, Canada. *In-situ* end labeling (ISEL) to identify regions of cell death, and CD31 immunolabeling to delineate vascularization were prepared at University Health Network Pathology Laboratory, Toronto, Canada. For analyses random regions of interest were chosen for each tumour and a normalized CD31-based vascular index (VI) was calculated. The VI was defined as the ratio of stained intact vessels to total vessels (including stained and unstained vessels).

Photoacoustic Imaging

Photoacoustic imaging to detect the oxygen saturation of blood was undertaken before and 24 hours after treatment using a Visual Sonics 2100 coupled to a visual Sonics LZR device (Visual Sonics, Toronto, Canada) (24). An LZ-250 transducer with a central frequency of 21 MHz and a gain of 20 dB was used for all imaging. Photoacoustic data obtained at two different wavelengths, 750 nm and 850 nm was used to determine deoxygenated and oxygenated haemoglobin. Twelve to fifteen slices were individually analyzed per tumour. The same regions of interest were used for all analyses.

Ultrasound Doppler Imaging

Doppler ultrasound imaging was carried out to detect blood flow in tumours before and 24 hours after treatment using a VEVO-770 (Visual Sonics, Toronto, Canada) with a central frequency of 25 MHz, and an RMV-710B transducer. Power doppler imaging was done using a wall filter of 2.5 mm/s, a step size of 0.2 mm, a scan speed of 2 mm/s, and a 20 dB gain setting. Power doppler data were analyzed to determine vascularization index defined as the relative volume occupied by doppler signal within a tumour volume (25) using MATLAB. Mice were anesthetized as for therapy and photoacoustic imaging.

Light Microscopy

For microscopy of specimens on slides, a Leica DC100 microscope was used with a 20X objective coupled to a Leica DC100 video camera wired to a 2 GHz PC running Leica IM1000 software (Leica GmbH, Germany). Cell death areas were quantified in histology and immunohistochemistry tumour sections assisted by the use of Image-J (NIH, USA) macroscopically to detect ISEL positive areas in tumour sections. At higher magnifications (40X) apoptotic cells were counted manually by identifying typical apoptotic bodies.

Statistical Analysis

Statistical analyses included one-way ANOVA testing of the ISEL, photoacoustics data and for the histological assessments of vasculature data. *T*-test analyses were also used to evaluate the significance of differences between the individual treatment conditions. Analysis of variance (ANOVA) was used to determine effects on the basis of variance. This is based on a comparison of variance between items to variance within items using a sum-of-squares approach to compute variances. A $P < 0.05$ was used to indicate statistical significance (Graph Pad/InStat 3.0, La Jolla, CA, USA).

Results

Treatments were undertaken as before with results indicating effects on vascular function in terms of photoacoustics data, blood flow as assessed by power doppler and photoacoustics. Figure 1 presents representative results of photoacoustics data in addition to corresponding power doppler data for selected treatment conditions. Photoacoustic imaging was undertaken of tumours treated with all experimental conditions, measuring oxygen saturation, and total haemoglobin. Data indicate changes in detectable blood flow most prominently with the combined treatment of ultrasound-stimulated microbubbles and 8 Gy radiation as before (2). More subtle changes in the total haemoglobin and oxygen saturation maps were apparent. Again the combined treatment condition of the ultrasound-stimulate microbubbles and 8 Gy appeared to cause a shift in detectable oxygen saturation toward deoxygenated values.

Photoacoustics data was assessed quantitatively averaging results over the tumour volumes. Significant decreases in oxygen saturation were observed across all treatment conditions where does of radiation and/or ultrasound-stimulated microbubbles were administered ($P < 0.05$), as measured by

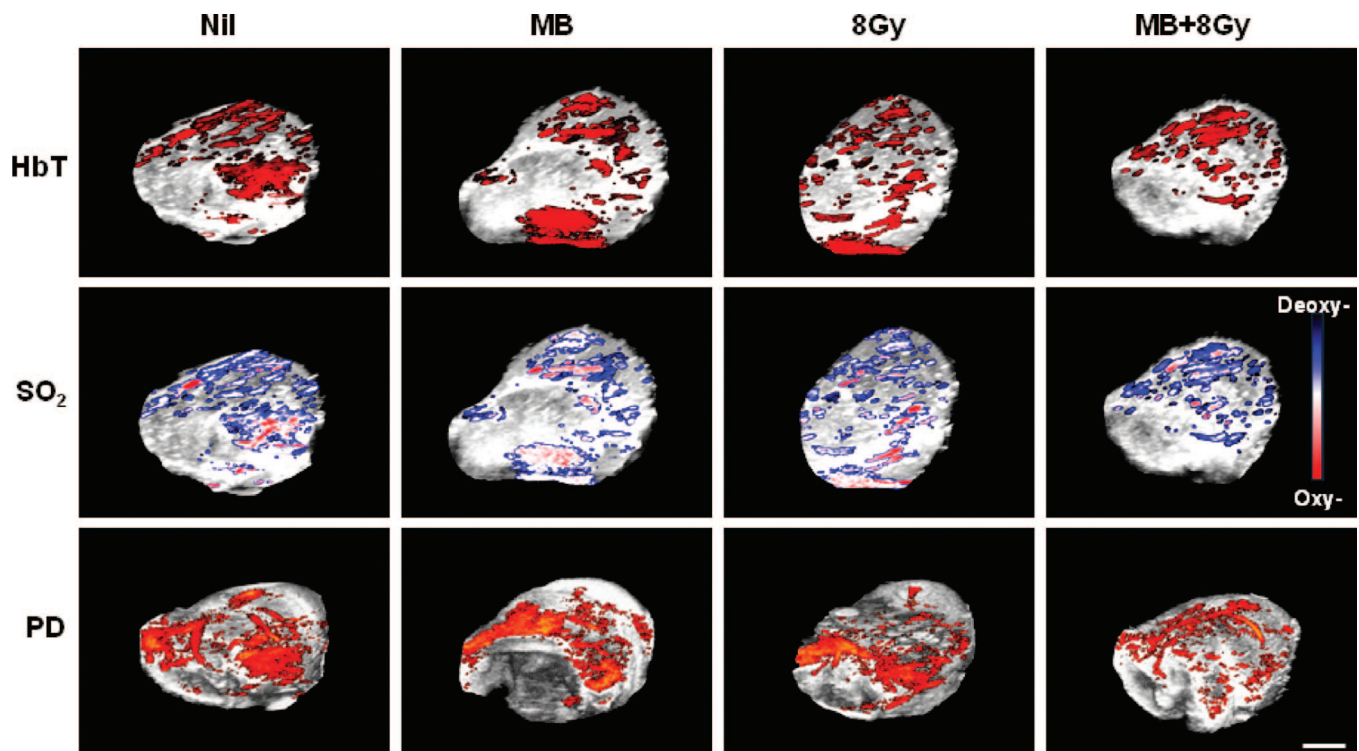


Figure 1: Photoacoustic and power doppler (PD) images for tumours treated with ultrasound-stimulated microbubbles (MB), radiation (8 Gy) or a combination of MB and 8 Gy. The images illustrate an overlay of the photoacoustic or doppler signals over 3D high-frequency B-mode ultrasound images. The upper panel shows the total haemoglobin signal (HbT), which was reduced as the stringency of the treatment increased. Similarly the middle panel illustrates a decrease in the level of oxygenated haemoglobin (SO_2); depicted as less red and more blue for the deoxygenated haemoglobin. The lower panel shows corresponding PD images. The scale bar indicates 2 mm.

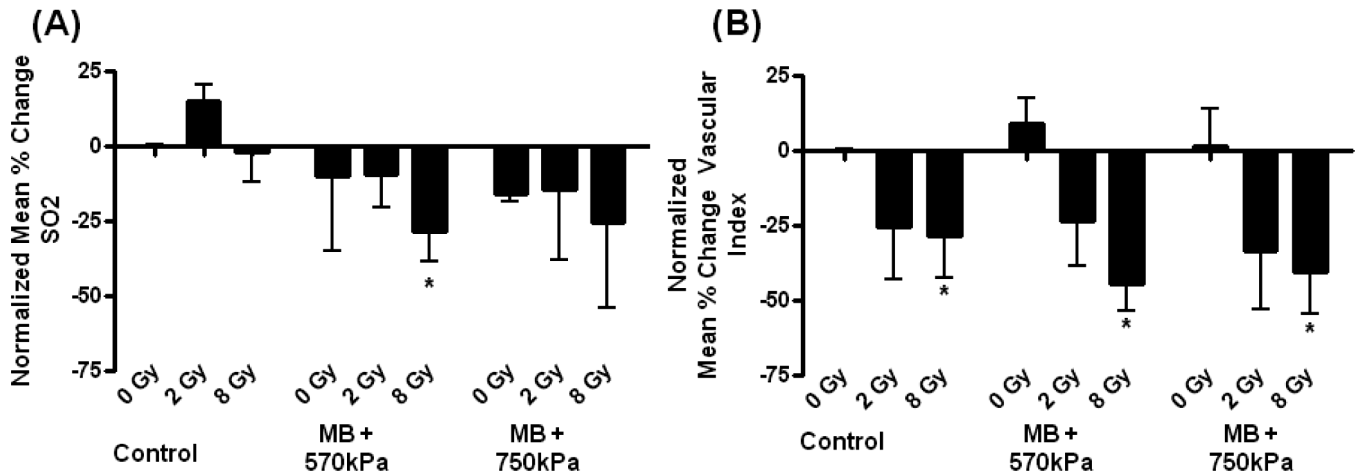


Figure 2: (A) Photoacoustic data showing percentage change in oxygen saturation (SO₂) per condition tested following treatment with a $P = 0.036$, using one-way ANOVA. (B) Power doppler data showing percentage change in blood flow per condition tested following treatment, where 8 Gy ($P < 0.0139$), MB (570 kPa) + 8 Gy ($P < 0.0011$), and MB (750 kPa) + 8 Gy ($P < 0.015$) were significantly reduced when compared to the control. The T -test was used to analyze photoacoustic and power doppler data. Asterisks indicate differences compare to control. Error bars indicate standard errors of the mean.

one-way ANOVA. Specific significant difference was also noted between control and 8 Gy combination group, 570 kPa ($P < 0.014$) (Figures 1 and 2). Total haemoglobin measures indicated similar trends, which were obvious but not significant (Figure S1).

Treatments using 8 Gy and microbubbles resulted in oxygen saturation decreasing by $28 \pm 10\%$ at 570 kPa and $25 \pm 29\%$ at 750 kPa, which corresponded to $44 \pm 9\%$ and $40 \pm 14\%$ respective decreases in blood flow as measured with power doppler. Corresponding histology indicated $31 \pm 5\%$ at 570 kPa and $37 \pm 5\%$ at 750 kPa in terms of tumour cell death in sectional histology. There were decreases in oxygen saturation which increased with increasing radiation dose and with increasing ultrasound pressure. Similar trends were observed with high-frequency power doppler measurement of blood flow.

Power doppler measures of blood flow indicated significant reductions in blood flow when 8 Gy radiation was included in the treatment condition (Figures 1 and 2). Treatments with 8 Gy alone ($P < 0.014$) and 8 Gy combined with ultrasound-stimulated microbubbles with both ultrasound pressures, 570 kPa ($P < 0.001$) and 750 kPa ($P < 0.0016$), were significantly reduced as compared to control (described above).

In order to investigate the implications of photoacoustic and power doppler findings further, standard histological staining and analyses of immunolabeling for cell death and vascular staining were undertaken. Specifically, ISEL and CD31 staining were undertaken to determine areas of cell death and intact vascular indices, respectively. Significant

differences in areas of cell death were detected across conditions (Figures 3 and 4) as measured by one-way ANOVA ($P < 0.05$). There were increases in cell death with increases in radiation dose and with increases in ultrasound pressures used with ultrasound-stimulated microbubble treatments. In samples treated with 8 Gy and ultrasound stimulated microbubbles there were pyknotic nuclei present as well as retraction artifact indicative of apoptotic cell death in central tumour regions.

Specific differences were also detected in comparing areas of cell death in the control group to four treatment conditions; the individual treatment condition of microbubbles perturbed at 750 kPa ($P < 0.011$) the combined treatment condition of microbubbles at 750 kPa and 2 Gy radiation ($P < 0.04$), and both conditions combining microbubbles and ultrasound pressure with 8 Gy radiation, 570 kPa ($P < 0.005$) and 750 kPa ($P < 0.002$) respectively. Significant changes in vascularization were confirmed by one-way ANOVA of CD31 staining results ($P < 0.05$) (Figure 5). Evaluations using T -tests also revealed significant differences for the treatment conditions combining 8 Gy radiation with microbubbles and ultrasound pressure at 570 kPa ($P < 0.033$) and 750 kPa ($P < 0.015$), as well as for the condition combining 2 Gy radiation with microbubbles and 570 kPa ($P < 0.039$). Areas of blanching were detected in the haematoxylin and eosin stained sections as visualized in our recent studies (2).

The strongest changes across all three treatment assessment modalities was found when combining 8 Gy of radiation with ultrasound-stimulated microbubbles at both pressures. We observed $28 \pm 10\%$ (570 kPa) and $25 \pm 29\%$ (750 kPa)

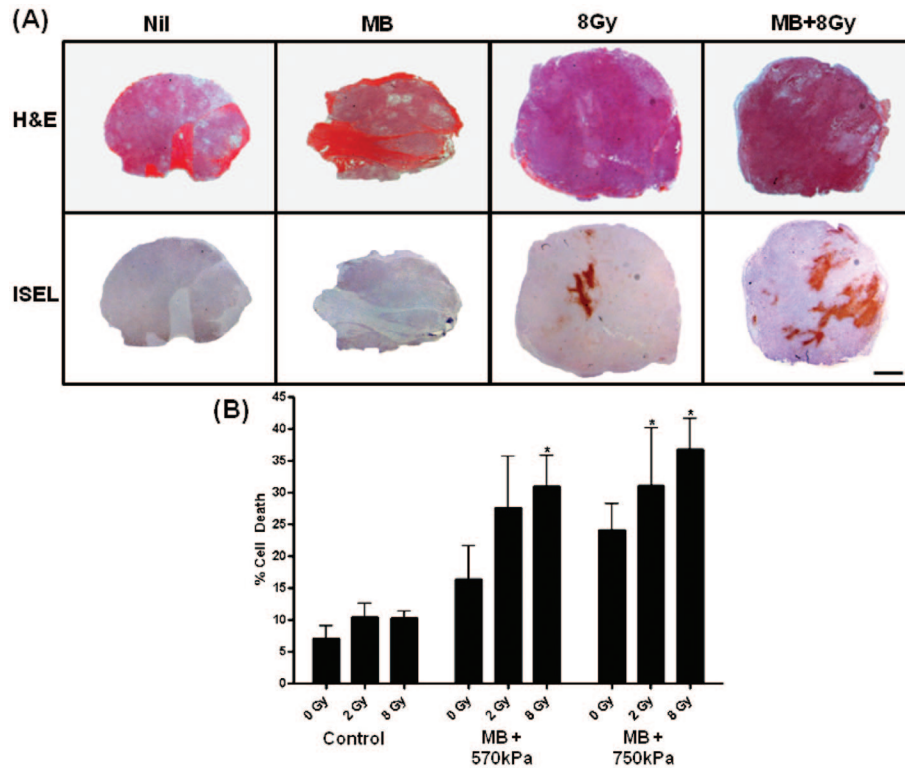


Figure 3: (A) Evaluation of cell death in representative sections of PC3 prostate mice xenograft tumours at low magnification. Haematoxylin and eosin (H&E, top row) and corresponding ISEL (bottom row) stained sections in rows. Columns represent conditions; no treatment (control), ultrasound-stimulated microbubbles with 750 kPa ultrasound only (MB), 8 Gy radiation only (XRT), and combined ultrasound-stimulated microbubble with 750 kPa and 8 Gy treatment. Control and MB samples demonstrate few diffuse areas of cell death. The 8 Gy treated sample demonstrates small diffuse areas of cell death with a large area of cell death centered in the middle. When microbubbles and radiation are combined, the areas of cell death appear enlarged and the center area of cell death becomes larger and more concentrated. Note the enhancement of cell death in the MB + 8 Gy treated tumours. (B) Data illustrating percentage of cell death, where one-way ANOVA testing indicated a significant difference with $P = 0.0103$. Specific differences were also observed using T -test, when comparing the combined treatments of MB (750 kPa) + 2 Gy ($P < 0.04$), MB (570 kPa) + 8 Gy ($P < 0.005$) and MB (750 kPa) + 8 Gy ($P < 0.002$) to the control. The scale bar indicates 1 mm. Error bars indicate standard error of the mean.

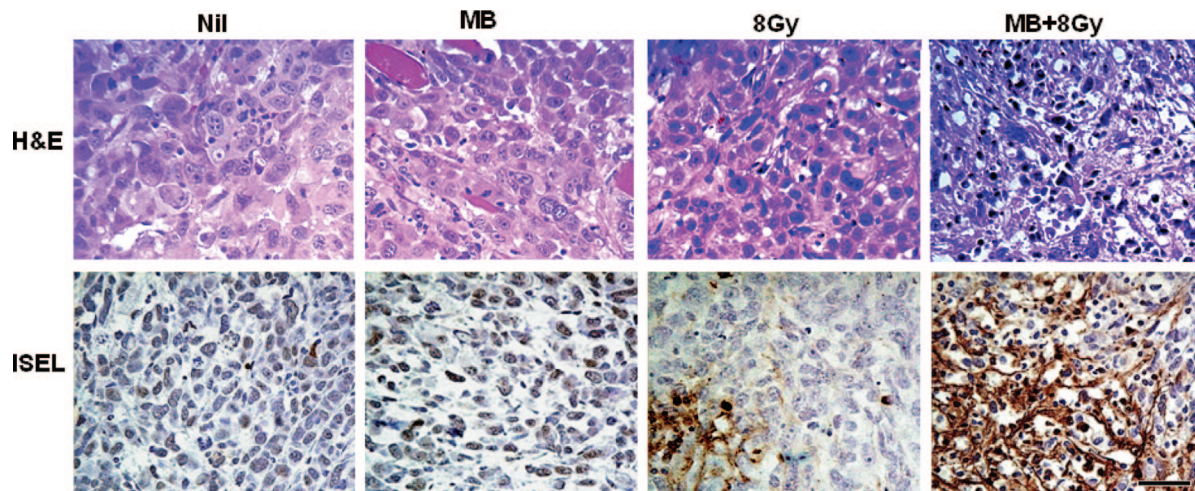


Figure 4: Evaluation of cell death in representative sections of PC3 prostate mice xenograft tumours at high magnification. Haematoxylin and eosin (H&E, top row) and corresponding ISEL (bottom row) stained sections in rows. Columns represent conditions as in other figures. Control & MB show non specific cytoplasmic staining and few diffuse areas of cell death. XRT shows small diffuse areas of cell death with a large area of cell death in the center left. When microbubbles and radiation are combined, the area of cell death becomes larger and more concentrated. Note the enhancement of cell death in the MB + XRT treated tumours. The scale bar indicates 50 μ m.

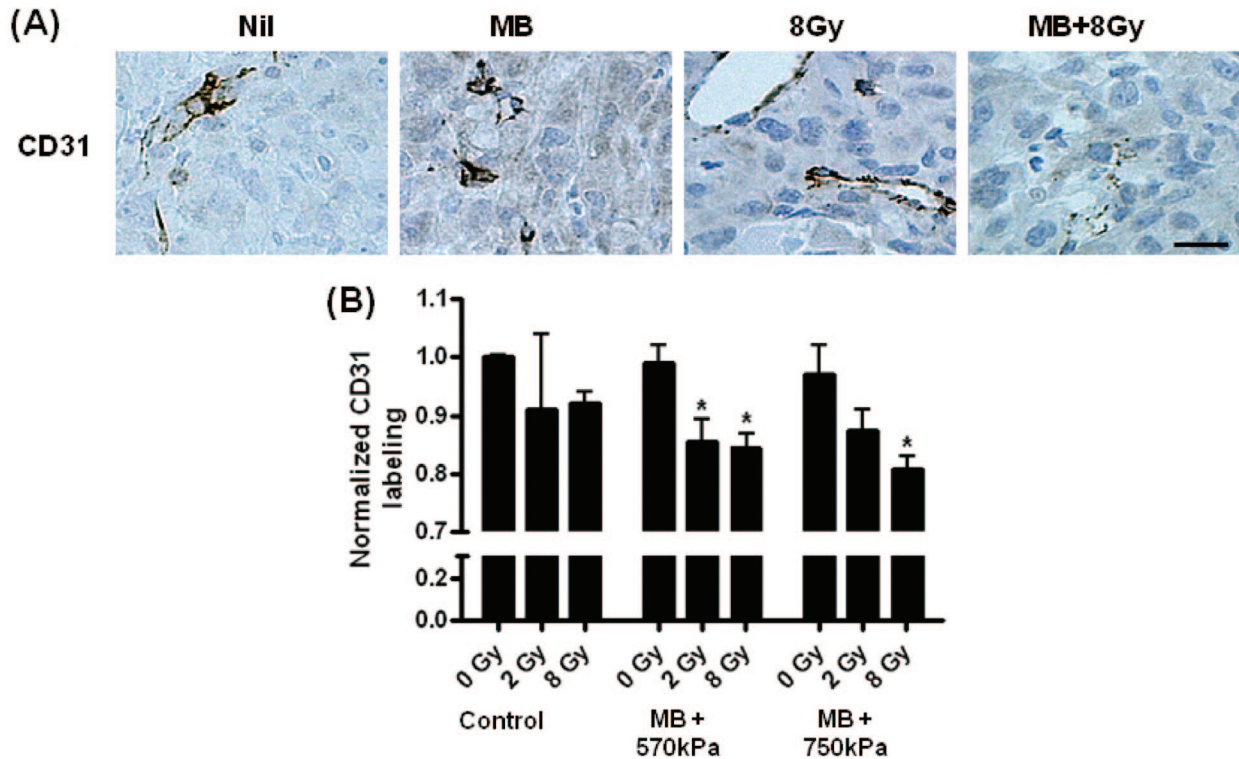


Figure 5: Histological evaluation of vasculature. (A) Endothelial cells lining intact vasculature were stained dark. Damaged endothelial cells do not stain as intensely due to membrane disruption. (B) One-way ANOVA testing revealed a $P = 0.0094$ for treatment effects, and specific differences were observed when using T -test to compare the combined treatments of MB (570kPa) + 2 Gy ($P < 0.039$), MB (570kPa) + 8 Gy ($P < 0.033$) and MB (750kPa) + 8 Gy ($P < 0.015$) to the control. The scale bar indicates 25 μ m.

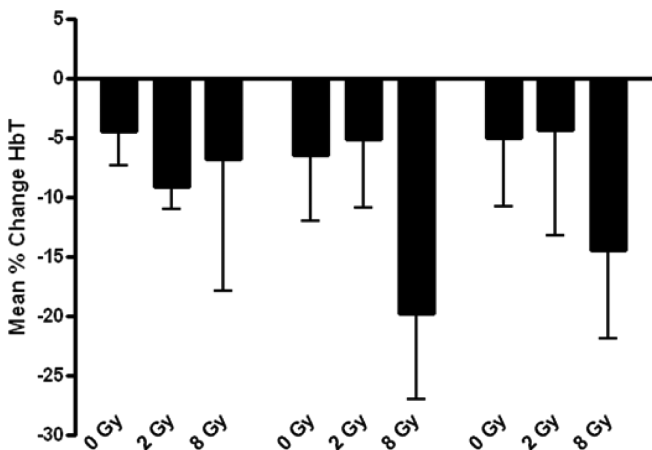


Figure S1: Photoacoustic data showing percentage change in Haemoglobin (HbT) per condition. Although there was some decrease in the total level of HbT, it was not significant.

decreases in oxygen saturation, which corresponded to a $44 \pm 9\%$ and $40 \pm 14\%$ respective decrease in blood flow as measured with power doppler. Corresponding immunolabeling indicated $15 \pm 2\%$ at 570kPa ($P < 0.033$) and $20 \pm 2\%$ at 750kPa ($P < 0.015$) decreases in intact vasculature, and $31 \pm 5\%$ at 570kPa ($P < 0.005$) and $37 \pm 5\%$ at 750kPa

($P < 0.002$) cell death as detected by ISEL staining. Control samples showed negligible changes with sham treatments. Changes in total haemoglobin mirrored changes in oxygen saturation but were less significant (Figure S1).

Discussion

In this study we used photoacoustic imaging to monitor tumour microvasculature responses to microbubble-enhanced radiation therapy. As hypothesized, treatment with a combination of ultrasound-stimulated microbubbles and radiation resulted in greater changes in oxygen saturation, total haemoglobin and blood flow than control and single treatments.

Power doppler imaging has been used previously to assess tumour responses to radiation combined with anti-angiogenics (13). Here it indicated significant decreases in blood flow when comparing control to 8 Gy treatment in combination with microbubbles at both 570kPa ($P < 0.001$) and 750kPa ($P < 0.015$). Furthermore, blood flow as measured by power doppler was significantly decreased in the 8 Gy condition, and comparable to the combined treatment at 750kPa ($P < 0.014$). However, there was appreciably more cell death in the combined treatments as indicated by immunohistochemistry. These findings reinforce the conclusion that

ultrasound-stimulated microbubbles significantly enhance radiation-induced cell death. The apparent synergy and mechanism behind this is described elsewhere but is linked to ceramide induction due to microbubble-induced cell membrane damage which results in vascular collapse when combined with radiation. Here we investigated the effect this phenomenon has on tumour microenvironment using photoacoustics.

Photoacoustic measures of total haemoglobin and oxygen saturation paralleled power doppler analyses of blood flow; oxygen saturation was found to be significantly different across treatment conditions ($P < 0.05$). Decreases in oxygen saturation were expected given these treatments appear to cause vascular disruption and decreases in power doppler detectable cell death. Evaluations were made at 24 hours after treatment where lack of blood flow would be expected to cause decreases in oxygen saturation and hypoxia. Although this occurs, repeated treatments (2) have been demonstrated to be more efficacious in terms of tumour growth inhibition and curability of tumours. It is likely that this is not relatively mild hypoxia which permits cellular viability and can inhibit radiation effects but a level of hypoxia consistent with vascular disruption causing tumour cell death centrally in tumours. The photoacoustic imaging carried out non-invasively here indicates progressive decreases in saturation with increasing radiation doses and increasing ultrasound-stimulated microbubble vascular perturbation. The photoacoustic measurement for samples treated with the highest insonifying peak-negative pressure demonstrated the greatest variability. This could be due to animal variability or a transient change in oxygen saturation related to the vascular destruction induced by treatments. Hypoxia has been recognized to have dynamic changes rather than being a static condition.

Photoacoustic and power doppler findings were supported by histological assessments of cell death and vascular indices. Significant decreases were detected in vascular indices, as measured by endothelial cell CD31 staining, and these findings were supported by increases in cell death as detected with ISEL. Significant differences were seen in vascular indices across treatment conditions ($P < 0.05$). Specific differences in vascular indices were also revealed when comparing combined treatments to control conditions; 8Gy combined with microbubbles at 570 kPa ($P < 0.033$) and 750 kPa ($P < 0.015$), and 2Gy combined with microbubbles at 570 kPa ($P < 0.039$). Significant differences in percentage of cell death were likewise seen across conditions ($P = 0.0103$). In comparing cell death measurements in control groups to several treatment conditions, specific differences were also observed; 8Gy combined with microbubbles at 570 kPa ($P < 0.005$) and 750 kPa ($P < 0.002$), and 2Gy combined with microbubbles at 750 kPa ($P < 0.04$).

We have previously demonstrated that vascular perturbation using ultrasound-mediated microbubbles enhances tumour responses to radiation (2), but photoacoustic monitoring of this effect is novel. Prior trials with this type of treatment centered on determining the efficacy of microbubbles, comparing these results with other reported anti-angiogenic treatments, and optimizing dose combinations. Tran *et al.* (4) established ultrasound-activated microbubbles to be effective anti-vascular agents, found that these anti-vascular effects increase the efficacy of radiation treatment, and showed that tumours did not show the vascular regeneration displayed in other anti-vascular treatments when treated with microbubbles and radiation (25). Further enhancement may be obtainable using targeted microbubbles. Nevertheless, in testing different combinations of microbubble concentrations, ultrasound pressures and radiation doses, Kim *et al.* concluded that while increasing microbubble concentrations and radiation doses results in increased cell death, this enhancement reaches a plateau as ultrasound peak negative pressure increases (26). In this type of treatment (2) hypoxia up to a certain level may desensitize tumour regions to radiation however above a threshold it causes death. With ultrasound-stimulated microbubble radiation enhancement vascular destruction starves a tumour of significant blood supply and tumour cell death ensues.

Those investigations utilized histological assessment of vascular disruption and cell death, and power doppler blood flow indicators to monitor treatment efficacy. Power doppler gives information about overall blood flow in an area and is sensitive to low flows, and other studies have likewise demonstrated the benefits of power doppler as a monitor of tumour blood flow in response to anti-vascular agents (27-30).

Power doppler has several limitations in imaging tumour microvasculature responses to treatment. These include generation of image artifacts brought about by tissue movement near blood vessels, subjectivity of filter parameters, and scatter signals formed by nearby tissues (14). If properly optimized, photoacoustics has the potential to complement power doppler as an imaging modality in this context. Sensitive to both flowing and static blood, photoacoustic imaging can overcome limitations of doppler in imaging tumour microvasculature. It can also provide additional physiological information useful in the clinical monitoring of anti-vascular treatments, such as total haemoglobin and blood oxygen saturation (15). As photoacoustic imaging does not depend on flow, it is not susceptible to artifacts caused by nearby tissue movement and can potentially indicate the haemoglobin levels present with vascular rupture. With power doppler, avoiding these artifacts in the clinical setting would require a high level of subject cooperation to limit movement, and could limit its usefulness in this context in a clinical setting. Imaging tumours near the heart or other pulsatile

organ would present further challenges (31). The resolution of photoacoustic imaging is likewise not limited by the subjective filter parameters of power doppler and scatter signals from nearby tissues (14). It is the potential of photoacoustics to overcome limitations of power doppler, and the increased scope of information it can provide which makes it such an attractive imaging modality for monitoring this type of treatment.

Monitoring radiation treatment responses is attractive clinically as predicting tumour response may facilitate early changes to or termination of the treatment regimen. This permits more patient specific dose combinations, optimizing tumour response while ensuring minimal toxicity to healthy tissue. While short-term monitoring is not routinely used in conjunction with cancer therapy, the possibility is being explored. Adaptive radiotherapy integrates daily images into radiation treatment, allowing for treatment plan modification in the form of field margin and treatment dose, and has been considered in head and neck, pelvic, prostate, and lung cancer patients (32). Change in uptake of fluorine-18 2-fluoro-2-deoxy-D-glucose (FDG) has been established by PET as a reliable indicator of tumour cell death, and has been used clinically to monitor response to treatment in soft tissue and musculoskeletal carcinomas (33). FDG-PET has also been investigated for use with non small cell lung carcinoma (34), and has been used in adaptive radiotherapy for improving dose coverage of cervical cancer patients (34). Uptake of ^{99m}Tc-HL91 has also been used to monitor tumour sensitivity and response to radiation therapy in mouse models (36, 37). Dual modality PET/CT has been successfully used in monitoring the response of gastrointestinal stromal tumours to imatinib (38). While these modalities offer the information required to individually tailor patients' treatment, issues of invasiveness and cost impede their implementation on a wider scale.

Despite these advances in cancer therapy monitoring, an inexpensive, fast, non-invasive modality has yet to be established as feasible for routine imaging. Photoacoustic monitoring of tumour microvasculature response to treatments of this type is a relatively novel modality, and represents a possibility for this type of routine imaging. Further work with microbubble-enhanced radiation therapy and other anti-vascular agents should incorporate photoacoustic imaging in conjunction with power doppler and histological assessment to optimize the technology and to ensure consistency in the imaging modality. In particular, investigating the usefulness of photoacoustic imaging with different cell lines and larger tumour sizes would be valuable, as tumour blood flow can vary across tumour types. Larger sample sizes and longer-term treatment regimes will also help determine the suitability of photoacoustics for this type of imaging in a clinical setting.

Acknowledgements

G. J. Czarnota is supported by a Cancer Care Ontario Research Chair in Experimental Therapeutics and Imaging. This research was supported by grants from the CDMRP, University of Toronto, and the Terry Fox Foundation. Funding enabling this research was also received from FED-DEV Ontario. The authors also thank Ms. Michelle Martin from comparative research at Sunnybrook for the technical support with the animal experiments.

References

1. Garcia-Barros M, Paris F, Cordon-Cardo C, Lyden D, Rafii S, Haimovitz-Friedman A, Fuks Z & Kolesnick R. Tumor response to radiotherapy regulated by endothelial cell apoptosis. *Science* 300, 1155-1159 (2003). PMID: 12750523
2. Czarnota GJ, Karshafian R, Burns PN, Wong S, Al Mahrouki A, Lee J, Caissie A, Tran W, Kim C, Furukawaa M, Wong E & Giles A. Tumour radiation response enhancement by acoustical stimulation of the vasculature. *PNAS* 109, 2033-2041 (2012). DOI: 10.1073/pnas.1200053109
3. Al-Mahrouki AA, Karshafian R, Giles A & Czarnota GJ. Bioeffects of ultrasound-stimulated microbubbles on endothelial cells: gene expression changes associated with radiation enhancement in vitro. *Ultrasound Med Biol* 38, 1958-1969 (2012). DOI: 10.1016/j.ultrasmedbio.2012.07.009
4. Tran WT, Iradji S, Sofroni E, Giles A, Eddy D & Czarnota GJ. Microbubble and ultrasound radioenhancement of bladder cancer. *Br J Cancer* 107, 469-476 (2012). DOI: 10.1038/bjc.2012.279
5. Nofiele JT, Karshafian R, Furukawa M, Al Mahrouki A, Giles A, Wong S & Czarnota GJ. Ultrasound-activated microbubble cancer therapy: ceramide production leading to enhanced radiation effect in vitro. *Technol Cancer Res Treat* 12, 53-60 (2013). PMID: 22905807
6. Stride E & Saffari N. Microbubble ultrasound contrast agents: a review. *Proc Instn Mech Engrs* 217, 429-447 (2003). PMID: 14702981
7. Unger E, Matsunaga T, McCreery T, Schumann P, Sweitzer R & Quigley R. Therapeutic applications of microbubbles. *Eur J Radiology* 42, 160-168 (2002). PMID: 11976013
8. Dijkmans P, Juffermans L, Musters R, Van Wamel A, Ten Cate F, Van Gilst W, Visser CA, De Jong N & Kamp O. Microbubbles and ultrasound: from diagnosis to therapy. *Eur J Echocardiography* 5, 245-256 (2004). PMID: 15219539
9. Ay T, Havaux X, Van Camp G, Campenelli B, Gisselu G, Pasquet A, Deneff JF, Melin JA & Vanoverschelde JL. Destruction of contrast microbubbles by ultrasound: effects on myocardial function, coronary perfusion pressure, and microvascular integrity. *JAHA* 104, 461-466 (2001). PMID: 11468210
10. Ferrara K, Pollard R & Borden M. Ultrasound microbubble contrast agents: fundamentals and application to gene and drug delivery. *Annu Rev Biomed Eng* 9, 415-447 (2007). PMID: 17651012
11. Kobayashi N, Yasu T, Yamada S, Kudo N, Kuroki M, Kawakami M, Miyatake K & Saito M. Endothelial cell injury in venule and capillary induced by contrast ultrasonography. *Ultrasound Med Biol* 28, 949-956 (2002). PMID: 12208339
12. Liu Z, Gao S, Zhao Y, Li P, Liu J, Li P, Tan K & Xie F. Disruption of tumour neovasculature by microbubble enhanced ultrasound: a potential new physical therapy of anti-angiogenesis. *Ultrasound Med Biol* 38, 253-261 (2012). DOI: 10.1016/j.ultrasmedbio.2011.11.007

13. El Kaffas A, Giles A & Czarnota GJ. Dose-dependent response of tumor vasculature to radiation therapy in combination with Sunitinib depicted by three-dimensional high-frequency power doppler ultrasound. *Angiogenesis* 16, 443-454 (2013). DOI: 10.1007/s10456-012-9329-2
14. Jiang Y, Harrison T, Ranasinghesagara J & Zemp R. Photoacoustic and high-frequency power doppler ultrasound biomicroscopy: a comparative study. *J Biomed Opt* 15, 056008-056008-8 (2010). DOI: 10.1117/1.3491126
15. Zhang HF, Maslov K & Sivaramakrishnan M. Imaging of haemoglobin oxygen saturation variations in single vessels in vivo using photoacoustic microscopy. *Appl Phys Lett* 90, 053901-3 (2007). DOI: 10.1063/1.2435697
16. Swearingen JA, Holan SH, Feldman MM & Viator JA. Photoacoustic discrimination of vascular and pigmented lesions using classical and Bayesian methods. *J Biomed Opt* 15, 016019 (2010). DOI: 10.1117/1.3316297
17. Kuzmina I, Diebele I, Jakovels D, Spigulis J, Valeine L, Kapostinsh J & Berzina A. Towards noncontact skin melanoma selection by multispectral imaging analysis. *J Biomed Opt* 16, 060502 (2011). DOI: 10.1117/1.3584846.
18. Ntziachristos V. Clinical translation of optical and optoacoustic imaging. *Philos Transact Ser A Math Phys Eng Sci* 369, 4666-4678 (1955). PMID: 22006913
19. Zhang HF, Maslov K, Stoica G & Wang LV. Functional photoacoustic microscopy for high-resolution and non-invasive in vivo imaging. *Nat Biotechnol* 7, 848-851 (2006). PMID: 16823374
20. Kruger RA, Lam RB, Reinecke DR, Del Rio SP & Doyle RP. Photoacoustic angiography of the breast. *Med Phys* 37, 6096-6100 (2010). PMID: 21158321
21. De la Zerda A, Paulus YM, Teed R, Bodapati S, Dollberg Y, Khuri-Yakub BT, Blumenkranz MS, Moshfeghi DM & Gambhir SS. Photoacoustic ocular imaging. *Opt Lett* 35, 270-272 (2010). DOI: 10.1364/OL.35.000270
22. Wang X, Pang Y, Ku G, Xie X, Stoica G & Wang L. Noninvasive laser-induced photoacoustic tomography for structural and functional in vivo imaging of the brain. *Nat Biotechnol* 7, 803-806 (2003). PMID: 12808463
23. Nemoto M, Nomura Y, Sato C, Tamura M, Houkin K, Koyanagi I & Hiroshi A. Analysis of optical signals evoked by peripheral nerve stimulation in rat somatosensory cortex: dynamic changes in haemoglobin concentration and oxygenation. *J Cereb Blood Flow Metab* 3, 246-259 (1999). PMID: 10078876
24. Needles A, Heinmiller A, Sun J, Theodoropoulos C, Bates D, Hirson D, Yin M & Foster F. Development and initial application of a fully integrated photoacoustic micro-ultrasound system. *IEEE Trans Ultrason Ferroelectr Freq Control* 5, 888-897 (2013). DOI: 10.1109/TUFFC.2013.2646
25. Huang YL, Kuo SJ, Hsu CC, Tseng HS, Hsiao YH & Chen DR. Computer-aided diagnosis for breast tumours by using vascularization of 3D power doppler ultrasound. *Ultrasound Med Biol* 25, 1607-1614 (2009). DOI: 10.1016/j.ultrasmedbio.2009.05.014
26. Kim HC, Al-Mahrouki A, Gorjizadeh A, Karshafian R & Czarnota GJ. Effects of biophysical parameters in enhancing radiation responses of prostate tumors with ultrasound-stimulated microbubbles. *Ultrasound Med Biol* 2013 Apr 30. DOI: pii: S0301-5629(13)00045-8. 10.1016/j.ultrasmedbio.2013.01.012. [Epub ahead of print] PMID: 23643061
27. Goertz DE, Yu JL, Kerbel RS, Burns PN & Foster FS. High frequency doppler ultrasound monitors the effects of antivascular therapy on on tumour blood flow. *Cancer Res* 62, 6371-6375 (2002). PMID: 12438217
28. Gee MS, Saunders HM, Lee JC, Sanzo JF, Jenkins WT, et al. Doppler ultrasound imaging detects changes in tumour perfusion during antivasculature therapy associated with vascular anatomic alterations. *Cancer Res* 61, 2974-2982 (2001). PMID: 11306476
29. Xuan JW, Bygrave M, Jiang H, Valiyeva F, Dunmore-Buyze J, Holdsworth DW, Izawa JI, Bauman G, Moussa M, Winter SF, Greegner NM, Chin JL, Drangova M, Fenster A & Laceyfield JC. Functional neoangiogenesis imaging of genetically engineered mouse prostate cancer using three dimensional power doppler ultrasound. *Cancer Res* 6, 2830-2839 (2007). PMID: 17363606
30. Hamper UM, De Jong MR, Caskey CI & Sheth S. Power doppler imaging: clinical experience and correlation with color coppler US and other imaging modalities. *Radiographics* 17, 499-513 (1997). PMID: 9084086
31. Cook GJ, Houston S, Barrington SF & Fogelman I. Technetium-99m-labeled HL91 to identify tumour hypoxia: correlation with fluorine-18-FDG. *J Nucl Med* 39, 99-103 (1998). PMID: 9443745
32. Lu W, Olivera GH, Chen Q, Ruchalal KJ, Haimer J, Meeks SL, Langen K & Kupelian PA. Deformable registration of the planning image (kVCT) and the daily images (MVCT) for adaptive radiation therapy. *Phys Med Biol* 51, 4357-4374 (2006). PMID: 16912386
33. Jones DN, McCowage GB, Sostman HD, Brizel DM, Layfield L, Charles HC, Dewhurst MW, Prescott DM, Friedman HS, Harrelson JM, Scully SP & Coleman RE. Monitoring of neoadjuvant therapy response of soft-tissue and musculoskeletal sarcoma using fluorine-18-FDG PET. *Journ Nucl Med* 37, 1438-1444 (1996). PMID: 8790188
34. Erdi Y, Macapinlac H, Rosenzweig K, Humm JL, Larson SM, Erdi AK & York ED. Use of PET to monitor the response of lung cancer to radiation treatment. *Eur J Nucl Med Mol Imaging* 27, 861-866 (2000). PMID: 10952499
35. Lin LL, Mutic S, Low DA, Laforest R, Vicic M, Zoberi I, Miller TR & Gigsby PW. Adaptive brachytherapy treatment planning for cervical cancer using FDG-PET. *Int J Radiat Oncol Biol Phys* 67, 91-96 (2007). PMID: 17189066
36. Suzuki T, Nakamura K, Kawase T & Kubo A. Monitoring of response to radiation therapy for human tumour xenografts using 99mTc-HL91 (4,9-diaza-3,3,10,10-tetramethyldodecan-2,11-dione dioxime). *Ann Nucl Med* 2, 131-138 (2003). PMID: 12790362
37. Yao Z, Qu W, Zhou Y, Zhu M & Zhu L. 99mTc-HL91 "hot spot" imaging of mice bearing human carcinoma by gamma camera and the effects of tumour necrosis on imaging. *Chin Med J (Engl)* 5, 404-407 (2000). PMID: 11776093
38. Antoch G, Kanja J, Bauer S, Kuehl H, Renzing-Koehler K, Schuette J, Bockisch A, Debatin JF & Freudenberg LS. Comparison of PET, CT, and dual-modality PET/CT imaging for monitoring of imatinib (STI571) therapy in patients with gastrointestinal stromal tumours. *J Nucl Med* 45, 357-365 (2004). PMID: 15001674

Received: March 28, 2013; Revised: May 30, 2013;

Accepted: June 5, 2013